PREDICTION OF BUILD GEOMETRY FOR DED USING SUPERVISED LEARNING METHODS ON SIMULATED PROCESS MONITORING DATA

Charles Snyers[1], Julien Ertveldt[1], Jorge Sanchez-Medina[1], Zoé Jardon[1,2] and Jan Helsen[1]

[1] Vrije Universiteit Brussel, Pleinlaan 2, 1050 Brussel, Belgium
[2]von Karman Institute for Fluid Dynamics, Waterloosesteenweg 72, 1640 Sint-Genesius-Rode, Belgium

Abstract

One of today's ongoing challenges in Directed Energy Deposition (DED) is controlling the geometry and material properties of parts. This manufacturing process is complex and non-linear due to multiple physical phenomena at play and is therefore hard to model analytically. Machine learning (ML) on the contrary is particularly well suited to predict the behavior of a complex process with multiple inputs and outputs such as DED.

A significant amount of data is required to train machine learning models but experimental data is costly time-wise and should therefore be produced in an intelligent way. As a stepping stone for the future production of experimental training data, a finite element model of the process was developed in this paper as a unlimited source of training data for the ML models. This model takes into account the printing parameters (laser speed, laser power and powder flow rate) and outputs simulated process monitoring data thanks to a post-processing method that is outlined in this paper. A dataset was produced by simulating 102 tracks in 316L stainless steel with the model. From analysis of this dataset, it was shown that K-Nearest Neighbors, Support Vector Regression, Decision Tree regression, linear regression and Artificial Neural Network models are all capable of modelling the relationship between the printing parameters and the melt pool characteristics effectively.

Introduction

Directed Energy Deposition

Directed Energy Deposition (DED) is a promising metal additive manufacturing process with applications in several high value industries such as aerospace and automotive. This process uses a high power laser beam to melt locally a metal workpiece. A nozzle blows fine metallic powder into the melt pool thanks to an inert carrier gas. The powder interacts and mixes with the molten substrate and the resulting material addition solidifies as the nozzle moves to create a track. A shielding gas is also blown around the melt pool to minimize oxidation of the melt pool. The printing head moves in 3 dimensions to stack tracks and ultimately create a part layer by layer.

Complexity of the DED process

There are several simultaneous physical phenomena at play during the DED process: radiative heat exchange between the laser and metal workpiece, liquid flow in the melt pool (induced by Marangoni forces), phase changes, powder and gas dynamics, etc [1], [2]. The thermal material properties add another layer of complexity since they generally are temperature-dependent. The process is therefore highly complex and non-linear. There are many printing parameters that have a first-order influence on the process: laser power, laser speed, powder feed rate, carrier gas flow, etc. In order to ensure repeatability and acceptable quality of the geometrical accuracy and material properties of parts, optimization of the printing parameters and control of the process are required.

Experimentally, monitoring the temperature distribution and the shape of the melt pool *in situ* provides relevant information to assess the properties of a part and optimize the process. Given the high temperature in the melt pool, a contactless method is necessary. Optical measurement of the emitted light by the melt pool allows the estimation of the temperature by using Planck's law and an estimation of the material emissivity. However, modelling the emissivity is another challenge on its own since it is a function of wavelength, temperature, phase, surface roughness and material composition [3].

In parallel, there have been a lot of effort to create numerical physics-based models of the DED process [4]–[6]. However, the ability of those models to predict experimental results is limited by the approximative knowledge of material properties [6] and by the difference in scale between a part and the melt pool dynamics which influence its microstructure [2].

Data-driven algorithms

In order to overcome the process non-linearities and the limitations of physics-based models, one can use data-driven methods to interpret raw experimental data and

build a surrogate model of the process without any inherent hypothesis on the melt pool dynamics or material properties.

Several different algorithms have been applied to DED or L-PBF monitoring data to do condition monitoring or process optimization. Li et al. [7] used a total of 211 melt pool infrared images to train a Convolutional Neural Network (CNN) to classify melt pool images according to their printing conditions. Khanzadeh et al. [8] applied the K-Nearest Neighbors (KNN), Support Vector Machine (SVM), Decision Tree (DT) and Discriminant Analysis (DA) methods to 1564 pyrometer melt pool images to detect the formation of porosities and compare the efficiency of each method. In a later paper, Khanzadeh et al. [9] applied the Self Organizing Map (SOM) algorithm to the same dataset to improve further the porosity detection. Caiazzo et al. [10] used the geometrical measurement of 120 DED tracks to train an three-layer Artificial Neural Network to predict the printing parameters.

Based on past work, it seems clear that there is a vast variety of data-driven algorithms currently available to researchers but there is no available method yet to determine *a priori* which will be the most adapted for a given application. Trial and error appears necessary to identify which algorithm to use and how much data it requires.

Cost of experimental data

Experiments on DED machines usually require specific safety measures because of the dangerous equipment at play (class 4 laser, inert gas flow). Moreover, it is necessary to label the collected dataset with measurements of the model target variable, for example by doing costly CT scans or metallographies to measure the track length or the presence of porosity. Collecting large datasets is therefore time-consuming.

It is then relevant to develop a source of artificial monitoring data able to sweep through many parameters quicker than experiments. With this artificial monitoring data one can preselect a good data-driven algorithm and determine how much data will be necessary to train it before doing a full scale experimental campaign.

In conclusion, this paper presents a finite element (FE) model of the DED process and a data post-processing method to produce artificial monitoring data. The first section of this work describes the FE model and the post-processing method. In the second section, the model and post-processing method are validated using past experimental results and a dataset of 102 artificial samples is produced. Finally, in the last section, the dataset is used to train several data-driven models of the DED process and their performance is compared in anticipation of an experimental campaign.

Simulation of the DED process

Thermal simulation and material addition

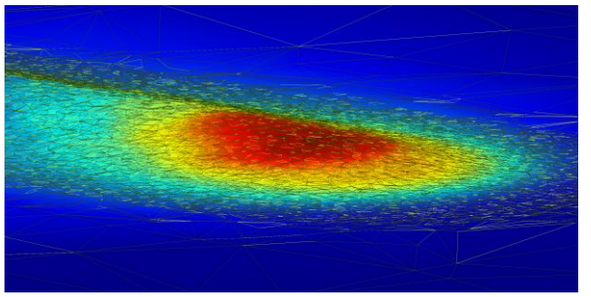

Figure 1 - 3D view of single-track thermal simulation with material addition

The numerical model developed for this work is based on the Nonlinear Transient Thermal class of the Morfeo numerical tool [11] by Cenaero, a research centre based in Gosselies, Belgium. It uses the extended finite element (FE) method combined with the level-set technique. The main advantage of this numerical tool is allowing material addition to the simulation without remeshing after every time-step.

The simulation solves the time-dependent heat equation in the 3-dimensional (x,y,z) space for 316L stainless steel with non-linear thermal properties (see Table 1 and 2):

$$\rho \frac{\partial h}{\partial t} = k\left(\frac{\partial^2 T}{\partial x^2} + \frac{\partial^2 T}{\partial y^2} + \frac{\partial^2 T}{\partial z^2}\right) \quad (1)$$

$$h = \int_{T_{ref}}^{T} c_p dT + f_l L_m \quad (2)$$

with T the temperature field, k the thermal conductivity, c_p the specific heat capacity, ρ the material density.

The enthalpy h takes the latent heat of fusion L_m into account thanks to a smooth liquid fraction function f_l as described by the developers of the numerical tool in a previous paper [1].

Table 1 - Temperature dependent material properties

T [K]	c_p [J/kg/K]	k [W/m/K]	ρ [kg/m^3]
300	434	13.96	7900
1000	498	24.96	-
1650	498	24.96	7900
1690	-	35.95	7430
2000	531	18.97	-
3000	600	22.25	-

Table 2 - Other simulation properties

L_m [kJ/kg]	α [-]	d [mm]	d_m [mm]	η [-]
270	0.45	1	1	0.33

The heat equation is solved in a rectangular domain representing a metal workpiece on which the additive process will take place. The mesh of the domain was obtained with Gmsh [12]. The domain is thermally isolated on all sides except the top one, where a moving flat-top laser heat flux $Q_h(x, y, t)$ is applied in analytical form [13]. No other heat boundary condition is imposed on the top side: thermal convection with air and thermal radiation are not taken into account to solve the heat equation.

$$Q_h(x', y) = \alpha \frac{2P}{\pi d^2} \frac{p 2^{\frac{2}{p}}}{\Gamma\left(\frac{2}{p}\right)} \exp\left(-2\left(\frac{\sqrt{x'^2 + y^2}}{\frac{d}{2}}\right)^p\right) \quad (3)$$

$$x' = x - vt \quad (4)$$

with P the laser power, v the laser speed, d the laser diameter, α the material absorptivity, and $p = 6$ the order of the flat top distribution.

Regarding the material addition, a level set function is defined at the beginning of the simulation to separate the activated part of the mesh where the heat equation is solved from the disabled part of the mesh. At every time-step the level set function is modified to reflect the material addition. Material is added according to a moving Gaussian distribution $Q_m(x, y, t)$:

$$Q_m(x', y) = \frac{\eta \dot{m}}{\rho} \frac{8}{\pi d_m^2} \exp\left(-2\frac{x'^2 + y^2}{\frac{d_m^2}{4}}\right) \quad (5)$$

$$x' = x - vt \quad (6)$$

with $\dot{m}$ the powder feed rate, η the powder efficiency and d_m the powder cone diameter.

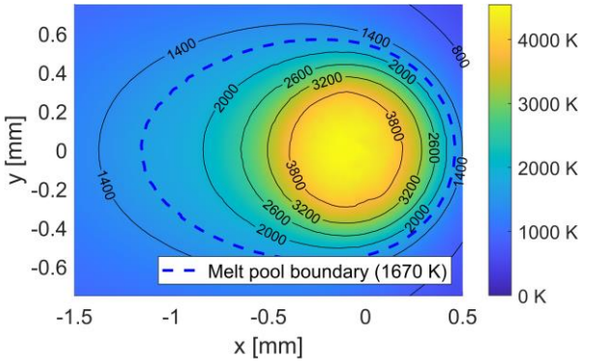

Figure 2 – Contour plot of $T(x, y, z)$ (P = 400W, v = 1000m/s and $\dot{m}$ = 1.5g/min)

To summarize, the simulation takes as input the 3 printing parameters (P, v, $\dot{m}$) and gives as output the temperature field $T(x, y, z)$. An example of temperature field computed by the simulation and viewed from the domain top side is in Figure 2.

From simulation to artificial monitoring data

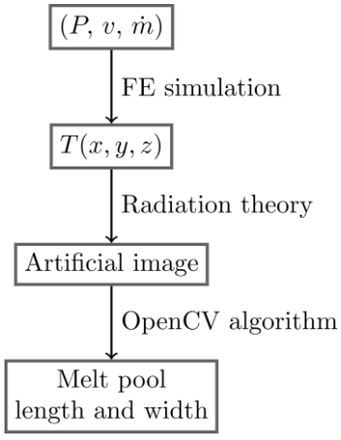

Figure 3 - Workflow of the post-processing method

The aim of the post-processing method is to transform the temperature field into artificial monitoring data that has the same format as experimental data and ultimately obtain the same geometrical information about the melt pool (see Figure 3). The experimental setup that is mimicked is the Micron precision Milling Closed-Loop

Additive (MiCLAD) research platform designed and built at the Vrije Universiteit Brussel [14]. This DED machine is equipped with several sensors, including a monochrome Basler acAC720-520um camera installed coaxially. The camera spectral relative response $S_\lambda(\lambda)$ is known from the camera documentation [15] and depicted in Figure 4.

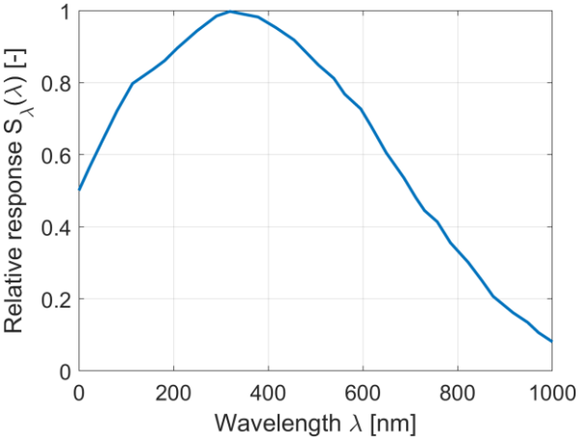

Figure 4 - Basler acAC720-520um spectral relative response [15]

First, the top side of the 3D temperature field $T(x,y,z)$ is projected onto a 2D plane that represents the point of view of the camera. The resulting 2D field is defined as $T_{cam}(x,y)$.

Then, the light emitted by the hot material can be computed with the temperature field and a few hypotheses. According to Planck's law [16], the spectral radiance B emitted by an ideal black body at temperature T is:

$$B(\lambda,T) = \frac{2hc^2}{\lambda^5}\frac{1}{\exp\left(\frac{hc}{\lambda k_B T}\right)-1} \qquad (7)$$

with k_B the Boltzmann constant, c the speed of light and h the Planck constant.

We assume the hot material to behave as a gray body with emissivity ϵ_λ independent from wavelength and that the head optics perfectly transmits the light from the melt pool to the camera. The spectral radiance L_λ [W/m^2/nm/sr] of the emitted light that is captured by the camera, is then:

$$L_\lambda(\lambda,x,y) = S_\lambda \times \epsilon_\lambda \times B\big(\lambda, T_{cam}(x,y)\big) \qquad (8)$$

We assume that the camera is equipped with a hypothetical lens which perfectly focuses all light rays coming from a point on the melt pool to a point on the camera sensor. Therefore the total irradiance $E(x,y)$ [W/m^2] that is incident to the camera sensor, is computed by integrating $L_\lambda(\lambda,x,y)$ over the camera wavelength range and over the solid angle ω of a hypothetical hemisphere h [17]:

$$E(x,y) = \int_{\lambda_1}^{\lambda_2}\iint_h L_\lambda(\lambda,x,y)\cos\theta\, d\omega\, d\lambda$$
$$= \int_{\lambda_1}^{\lambda_2}\int_0^{2\pi}\int_0^{\frac{\pi}{2}} L_\lambda(\lambda,x,y)\cos\theta\sin\theta\, d\theta\, d\phi\, d\lambda$$
$$= \pi\int_{\lambda_1}^{\lambda_2} L_\lambda(\lambda,x,y)\, d\lambda \qquad (9)$$

To build an artificial image from the captured power field, a 3x3 mm^2 region of the field around the melt pool is interpolated to a 260x260 grid which corresponds to the size of the Basler camera. Then, the grid float values are converted to 8-bit integers which represent the gray values of the artificial image. The gray values are scaled so that the captured power of the melting temperature (1670K) corresponds to the maximum intensity value (255) and the minimum captured power over the image corresponds to the minimum intensity value (0). This is equivalent to set the camera's exposure time to a value that saturates the pixel if the temperature is equal or above the melting temperature.

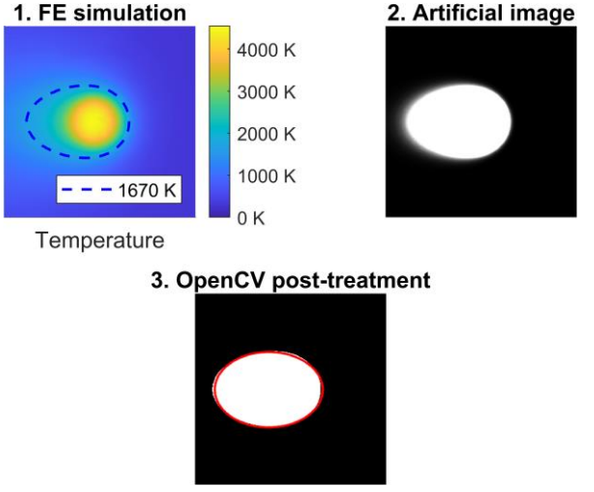

Figure 5 - Comparison of the melt pool temperature field, the artificial image and the result of the ellipse-fitting OpenCV algorithm

Finally, the artificial image is fed to a segmentation and fitting algorithm implemented with OpenCV [18]. First, it converts the grayscale image to a binary image by using a statistical-based Otsu thresholding algorithm. Then, the Suzuki's contour algorithm is applied to extract the boundary points of the melt pool. Finally, an ellipse is fitted to the boundary points by using the

Fitzgibbon method [18], i.e. by solving a least squares problem. The major and minor axes of the fitted ellipse are extracted as the length and width of the melt pool.

To summarise, the post-processing method takes the temperature field $T(x, y, z)$ as input and outputs two scalar values (l_{MP}, w_{MP}): the length and width of the melt pool. Figure 5 illustrates the evolution from the temperature field to the final fitted ellipse.

Simulated dataset

A set of 102 tracks in 316L stainless steel was simulated using the numerical tool method described in the previous section.

The printing parameters $(P, v, \dot{m})$ were chosen according to the following:

- The variation of each printing parameter must be sufficient for the data-driven algorithms to detect a non-linear behavior: at least 4 different values per printing parameter.
- The specific energy $E_d = P/(v \times d)$ of each parameter set ranges from 10 to 45 J/mm^2.

The values used for each parameter are respectively (not all combinations were simulated):

- P: 200, 300, 320, 360, 400, 500 and 600 W
- v: 800, 900, 1000, 1100 and 1200 mm/min
- $\dot{m}$: 0, 0.75, 1.5, 2.25 and 3 g/min

The dynamic model of the DED process can be approximated by a first order transfer function [19] with time constant τ:

$$G(s) = \frac{K}{1 + \tau s} \tag{10}$$

Each track was simulated for 0.2s, which is approximatively 5 times the time constant in the worst case for the considered range of printing parameters [19]. The laser moves in a straight line. Therefore the overall length of the trajectory ranges from 2.67mm to 4mm depending on the laser speed. The final time-step of each simulation is then supposed to reach steady-state and is used to extract the temperature field for each combination of printing parameters.

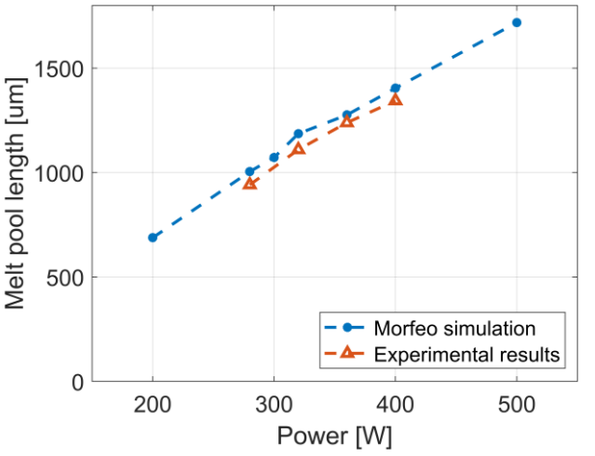

Figure 6 - Comparison of the melt pool length measured by the visual method from simulated and experimental datasets [18] ($\dot{m} = 3g/min$)

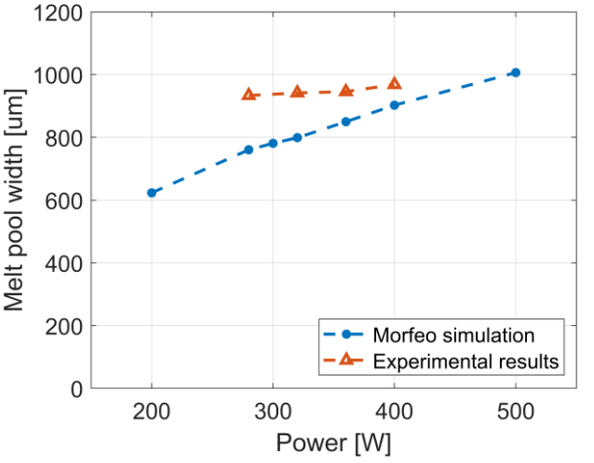

Figure 7 - Comparison of the melt pool width measured by the visual method from simulated and experimental datasets [18] ($\dot{m} = 3g/min$)

In order to validate the simulated results, they are compared with past experimental results obtained with the same segmentation and fitting algorithm developed by Medina et al [18]. Those experimental results were obtained by printing tracks of 30mm with 316L steel powder. Figures 6 and 7 show the comparison of the melt pool length and width obtained by simulated and experimental data for increasing laser power. It is observed that simulated and experimental results are in good agreement and this suggests that the simulation and post-processing method produce realistic data.

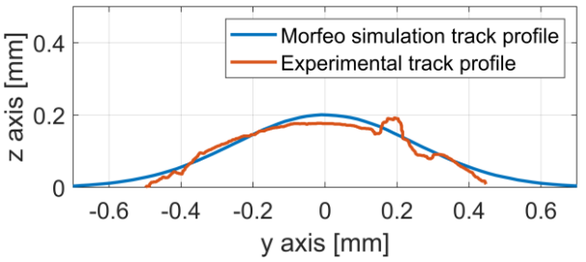

Figure 8 - Comparison of the track profiles from simulated and experimental datasets [20] ($P = 320W;\ v = 1000mm/min;\ \dot{m} = 3g/min$)

The single track cross-sectional profile of the simulated data is also compared on Figure 8 to a track profile obtained with the same process parameters and measured with a laser triangulation scanner by Jardon et al. [20]. It clearly shows that the simulated track and experimental track have very close deposition shape.

Prediction of the melt pool dimensions

Supervised Learning methods

In order to build a mathematical model of the relationship between printing parameters and the melt pool dimensions, Supervised Learning regression algorithms will be used because of the continuous nature of the output variables (melt pool length and width). As explained in the introduction, a trial and error step is necessary to determine which algorithm is the most adapted to the phenomenon to be modelled. In this paper we consider a selection of the most usual Machine Learning (ML) algorithms [21], as well as a simple example of Artificial Neural Network (ANN). The algorithms and their hyperparameters are listed in Table 3. The relationship that is approximated by the algorithms is the following:

$$(P, v, \dot{m}) \rightarrow l_{MP} \tag{11}$$

When fitting an algorithm to a given dataset, there is a risk of overfitting the algorithm to the particular set of available data and miss the general trend of the phenomenon. In this case, the resulting model will fail to predict future observations reliably [21]. To avoid it, the available dataset is usually split in two: the training set and the testing set. The training set is used to fit the algorithm and the testing set is used to evaluate its performance. An algorithm is optimally fitted when it minimizes the performance metrics over the testing set. There is still a risk that the particular choice of training and testing sets will lead to a selection bias. To avoid this second problem, we perform k-fold cross validation (CV) by splitting the dataset k times and checking the performance of the model on all the (training set, testing set) pairs.

Table 3 - Supervised Learning algorithms

Model	Hyperparameter(s)	Value
K-Nearest Neighbors	# of neighbors Weights	5 Uniform
Linear regression	-	-
Support Vector Regression	Kernel function Polynomial degree Kernel coefficient	RBF 3 Scaled
Decision Tree regression	Criterion	MSE
Artificial Neural Network	# of hidden layers Type of layer # of nodes per layer	3 Dense 1000

In order to evaluate the performance of the algorithms, we use two different metrics: the R^2 score and the Root Mean Square Error (RMSE). As explained, they are evaluated over the testing set.

$$R^2 = 1 - \frac{\sum_{n=1}^{N}(\hat{y}_n - y_n)^2}{\sum_{n=1}^{N}(\bar{y} - y_n)^2} \tag{12}$$

$$RMSE = \sqrt{\frac{\sum_{n=1}^{N}(\widehat{y_n} - y_n)^2}{N}} \tag{13}$$

with N the number of values in the set, y_n the n-th value in the set, $\hat{y}_n$ the algorithm predicted value and $\bar{y}$ the mean value of the set.

The R^2 score can be interpreted as the percentage of variance of the testing set that is captured by the model. A value of 1 means that the model perfectly represents the testing set.

Results and discussion

The algorithms presented in the previous subsection were implemented with *Scikit-Learn* and *Keras* Python packages [22], [23]. They were fitted to the simulated dataset on a Core i7-9850H laptop with 5-fold validation for the ML algorithms and 100 epochs for the ANN. The mean value was computed out of the 5 values of the 5-fold CV for the ML algorithms and the best value was kept out of the 100 epochs for the ANN.

Table 4 - Metrics of Supervised Learning algorithms fitted to simulated dataset

Model	R^2 [-]	RMSE [mm]	Training time [ms]
KNN	0.8268	0.1084	0.4
Linear regression	0.7703	0.1209	0.6
SVR	0.8273	0.1060	0.6
DT regression	0.8947	0.0841	0.2
ANN	0.8101	0.1257	5385.1

The resulting metrics and training times are listed in Table 4 and corresponding regression plots are shown in Figure 9. We can observe that the DT regression is the most effective model. An order of magnitude of a 100 samples seems satisfactory for such methods.

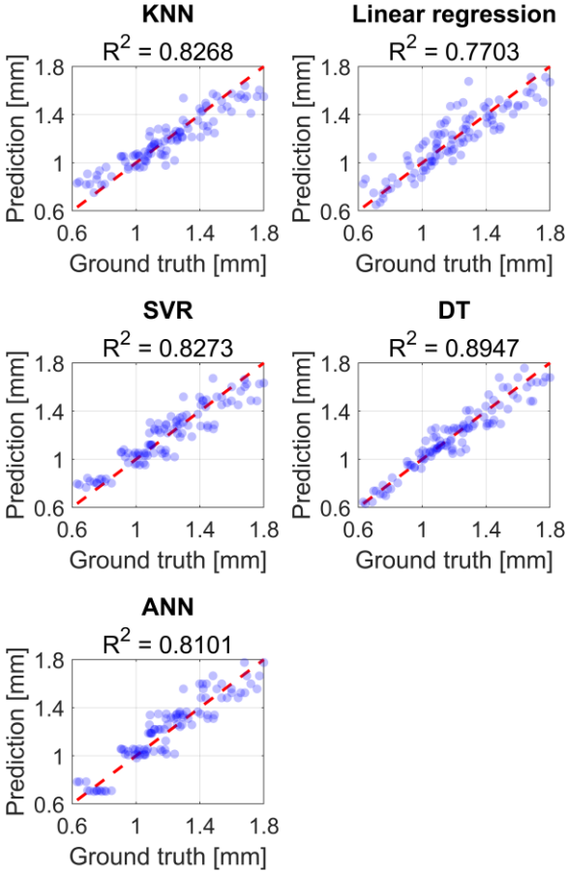

Figure 9 – Regression plots of Supervised Learning algorithms

The ANN is generally considered more able than traditional ML algorithms to generalize high-dimensional data [24]. Despite this, the ANN fitted to the simulated dataset has a lower R^2 score and higher RSME than the DT algorithm. One possible explanation could be the relatively limited size of the dataset. Indeed, the downside of a much more plastic model such as the ANN is that it requires much more data to fit efficiently all his internal weights and avoid a high model variance. Another possible explanation is that the structure of considered ANN is not appropriate to model the target relationship. In order to investigate these possibilities, a larger dataset should be produced and several ANN structures should be evaluated.

Moreover, it is clear that the training time is significantly higher for the ANN than for other algorithms. In the case of a shallow neural network and a relatively small dataset such as the ones considered in this work, the training time poses no issue but might be a problem for larger datasets or deeper networks.

It should be noted that neither the ANN's or the other algorithms' hyperparameters were optimized in this work. It is very likely that such optimization could lead to a better model.

Conclusion

In this paper, a FE simulation of the DED process and a novel method to produce artificial DED monitoring data were described. They were used to produce a dataset of 102 artificial images that links printing parameters and melt pool geometrical properties. It was observed that experimental data obtained in a similar fashion is in good agreement with the simulated dataset.

This multi-input, multi-output dataset was used to train several Supervised Learning regression models and their performances were compared. The results suggest that the relationship between printing parameters and the steady-state melt pool length can be approximated adequately by ML algorithms such as the Decision Tree regression. An order of magnitude of a 100 samples seems satisfactory for such algorithms. The Artificial Neural Network might either require more data or a different structure to be more performant than more traditional ML algorithms.

For future work, the production of artificial monitoring data could be used to consider more complex regression problems, such as the prediction of transient melt pool geometry or the thermal distribution, and the influence of the gas parameters on the melt pool geometry. In that case, the optimization of the algorithms' hyperparameters might be necessary to reach satisfactory performance.

Acknowledgements

The authors would like to acknowledge the support of the Flemish Government (AI Research Program).

References

[1] J. S. Cagnone, K. Hillewaert, and N. Poletz, 'A Discontinuous Galerkin Method for Multiphysics Welding Simulations', *KEM*, vol. 611–612, pp. 1319–1326, May 2014, doi: 10.4028/www.scientific.net/KEM.611-612.1319.

[2] W. Yan *et al.*, 'Data-driven multi-scale multi-physics models to derive process–structure–property relationships for additive manufacturing', *Comput Mech*, vol. 61, no. 5, pp. 521–541, May 2018, doi: 10.1007/s00466-018-1539-z.

[3] M. Lison, W. Devesse, D. de Baere, M. Hinderdael, and P. Guillaume, 'Hyperspectral and thermal temperature estimation during laser cladding', *Journal of Laser Applications*, vol. 31, no. 2, p. 022313, May 2019, doi: 10.2351/1.5096129.

[4] E. Toyserkani, A. Khajepour, and S. Corbin, 'Three-dimensional finite element modeling of laser cladding by powder injection: Effects of powder feedrate and travel speed on the process', *Journal of Laser Applications*, vol. 15, no. 3, pp. 153–160, Aug. 2003, doi: 10.2351/1.1585087.

[5] L. Yang *et al.*, 'Additive Manufacturing Process Chain', in *Additive Manufacturing of Metals: The Technology, Materials, Design and Production*, Cham: Springer International Publishing, 2017, pp. 33–43. doi: 10.1007/978-3-319-55128-9_2.

[6] Y. Huang, M. B. Khamesee, and E. Toyserkani, 'A new physics-based model for laser directed energy deposition (powder-fed additive manufacturing): From single-track to multi-track and multi-layer', *Optics & Laser Technology*, vol. 109, pp. 584–599, Jan. 2019, doi: 10.1016/j.optlastec.2018.08.015.

[7] X. Li, S. Siahpour, J. Lee, Y. Wang, and J. Shi, 'Deep Learning-Based Intelligent Process Monitoring of Directed Energy Deposition in Additive Manufacturing with Thermal Images', *Procedia Manufacturing*, vol. 48, pp. 643–649, Jan. 2020, doi: 10.1016/j.promfg.2020.05.093.

[8] M. Khanzadeh, S. Chowdhury, M. Marufuzzaman, M. A. Tschopp, and L. Bian, 'Porosity prediction: Supervised-learning of thermal history for direct laser deposition', *Journal of Manufacturing Systems*, vol. 47, pp. 69–82, Apr. 2018, doi: 10.1016/j.jmsy.2018.04.001.

[9] M. Khanzadeh, S. Chowdhury, M. A. Tschopp, H. R. Doude, M. Marufuzzaman, and L. Bian, 'In-situ monitoring of melt pool images for porosity prediction in directed energy deposition processes', *IISE Transactions*, vol. 51, no. 5, pp. 437–455, May 2019, doi: 10.1080/24725854.2017.1417656.

[10] F. Caiazzo and A. Caggiano, 'Laser Direct Metal Deposition of 2024 Al Alloy: Trace Geometry Prediction via Machine Learning', *Materials*, vol. 11, no. 3, Art. no. 3, Mar. 2018, doi: 10.3390/ma11030444.

[11] *Morfeo version 3.3.0 (2021), a Manufacturing ORiented Finite Element sOftware*. 2021. [Online]. Available: http://www.cenaero.be

[12] C. Geuzaine and J.-F. Remacle, 'Gmsh: A 3-D finite element mesh generator with built-in pre-and post-processing facilities', *International journal for numerical methods in engineering*, vol. 79, no. 11, pp. 1309–1331, 2009.

[13] J. A. Hoffnagle and C. M. Jefferson, 'Design and performance of a refractive optical system that converts a Gaussian to a flattop beam', *Appl. Opt., AO*, vol. 39, no. 30, pp. 5488–5499, Oct. 2000, doi: 10.1364/AO.39.005488.

[14] J. Ertveldt, P. Guillaume, and J. Helsen, 'MiCLAD as a platform for real-time monitoring and machine learning in laser metal deposition', in *Procedia CIRP*, 2020, p. 6.

[15] 'Basler acA720-520um documentation'. https://docs.baslerweb.com/aca720-520um (accessed Sep. 15, 2021).

[16] M. Planck, *Vorlesungen über die Theorie der Wärmestrahlung*. JA Barth, 1913.

[17] T. L. Bergman, A. Lavine, F. P. Incropera, and D. P. Dewitt, *Fundamentals of heat and mass transfer*. John Wiley & Sons New York, 2017.

[18] J. S. Medina, W. Devesse, J. Ertveldt, and P. Guillaume, 'Comparison of visual and hyperspectral monitoring of the melt pool during Laser Metal Deposition', *Procedia CIRP*, p. 6, 2020.

[19] M. Akbari and R. Kovacevic, 'Closed loop control of melt pool width in robotized laser powder–directed energy deposition process', *Int J Adv Manuf Technol*, vol. 104, no. 5, pp. 2887–2898, Oct. 2019, doi: 10.1007/s00170-019-04195-y.

[20] Z. Jardon, J. Ertveldt, and P. Guillaume, 'Effect of coaxial powder nozzle jet process parameters on single-track geometry for Laser Beam Directed Energy Deposition process', presented at the ASTM International Conference on Additive Manufacturing, 2021.

[21] T. Hastie, R. Tibshirani, and J. Friedman, *The Elements of Statistical Learning*. New York, NY: Springer New York, 2009. doi: 10.1007/978-0-387-84858-7.

[22] F. Pedregosa *et al.*, 'Scikit-learn: Machine learning in Python', *Journal of Machine Learning Research*, vol. 12, pp. 2825–2830, 2011.

[23] F. Chollet and others, 'Keras', 2015. https://github.com/fchollet/keras
[24] I. Goodfellow, Y. Bengio, and A. Courville, *Deep Learning*. MIT Press, 2016.

Meet the authors

Charles Snyers received his Master's degree in Electromechanical Engineering from Université Catholique de Louvain in 2016. In 2020 he joined the Department of Mechanical Engineering (MECH) of the Vrije Universiteit Brussel where he is currently a PhD student in the Additive Manufacturing Research Lab. His main research interests include Additive Manufacturing and Machine Learning.

Julien Ertveldt obtained the degree of Ph.D. in Engineering from the Vrije Universiteit Brussels (VUB). From 2018 he is working as a research engineer at the VUB Department of Mechanical Engineering on the development of integrated hybrid CNC machining systems combining Laser Metal Deposition, laser ablation and milling.

Jorge Sanchez Medina started pursuing a Ph.D. in 2019 at the Vrije Universiteit Brussel, Belgium. He received his M.Sc. degree in Telecommunications Engineering in 2011 from the Universidad de Las Palmas de Gran Canaria, Spain. From 2011 to 2019 he worked as engineer in different fields and European countries, where he spent most of his time in the automotive industry in Germany.

Zoé Jardon was born in Uccle, Belgium, in 1993. She received the degree in electro-mechanical engineering in 2016. In 2017 she joined the Department of Mechanical Engineering (MECH) of the Vrije Universiteit Brussel where she is currently a Ph.D. researcher in the Additive Manufacturing Research Group in collaboration with the von Karman Institute. Her main research interests are situated in the field of fluid dynamics, aeroacoustics, Structural Health Monitoring and Additive Manufacturing.

Jan Helsen received the M.Sc. degree in Electromechanical Engineering and the Ph.D. degree from Katholieke Universiteit Leuven, Leuven, Belgium, in 2007 and 2012, respectively. His Ph.D. thesis was focused on the dynamic simulation of wind turbine gearboxes. He is currently a Professor with the Acoustics and Vibrations Research Group, Vrije Universiteit Brussel, Brussel, Belgium. His current research interest includes condition monitoring of rotating systems.

AIP Publishing

LIA THE LASER INSTITUTE

Journal of Laser Applications

ACCEPTED MANUSCRIPT

PLEASE CITE THIS ARTICLE AS DOI: 10.2351/7.0000526

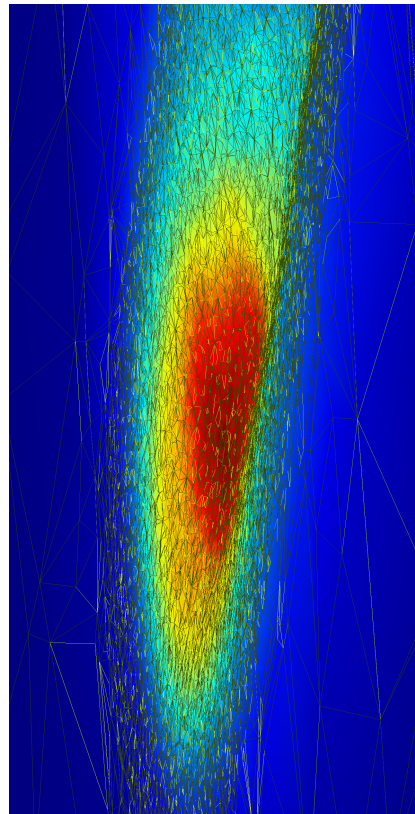

AIP Publishing
ALIA THE LASER INSTITUTE
Journal of Laser Applications
ACCEPTED MANUSCRIPT

PLEASE CITE THIS ARTICLE AS DOI: 10.2351/7.0000526

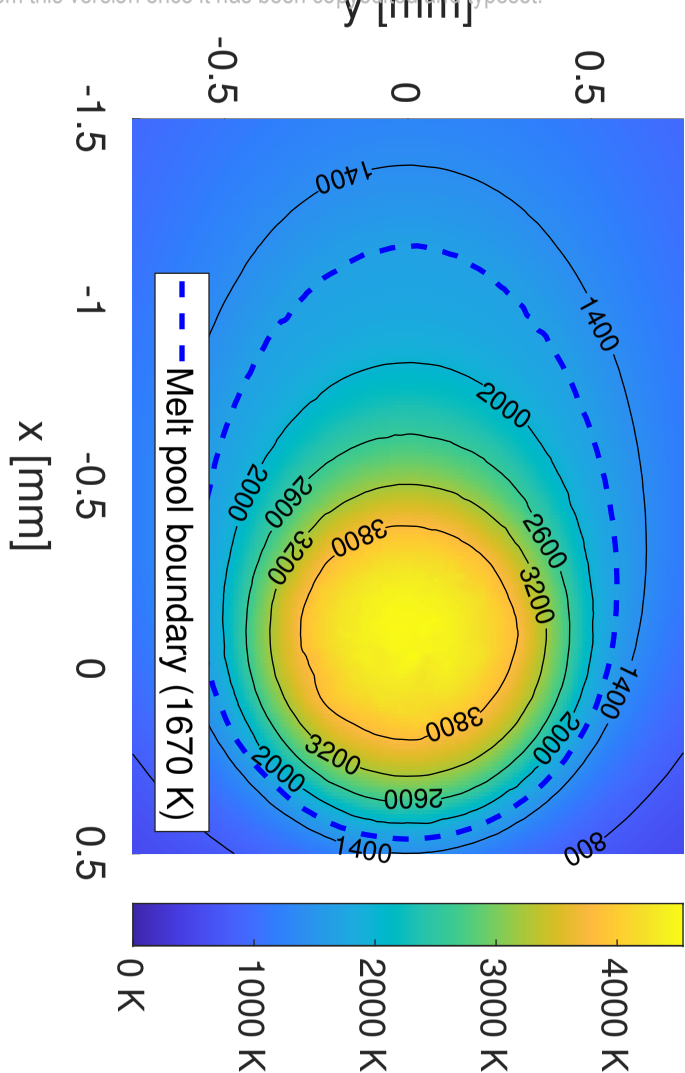

AIP Publishing
ALIA THE LASER INSTITUTE
Journal of Laser Applications
ACCEPTED MANUSCRIPT

PLEASE CITE THIS ARTICLE AS DOI: 10.2351/7.0000526

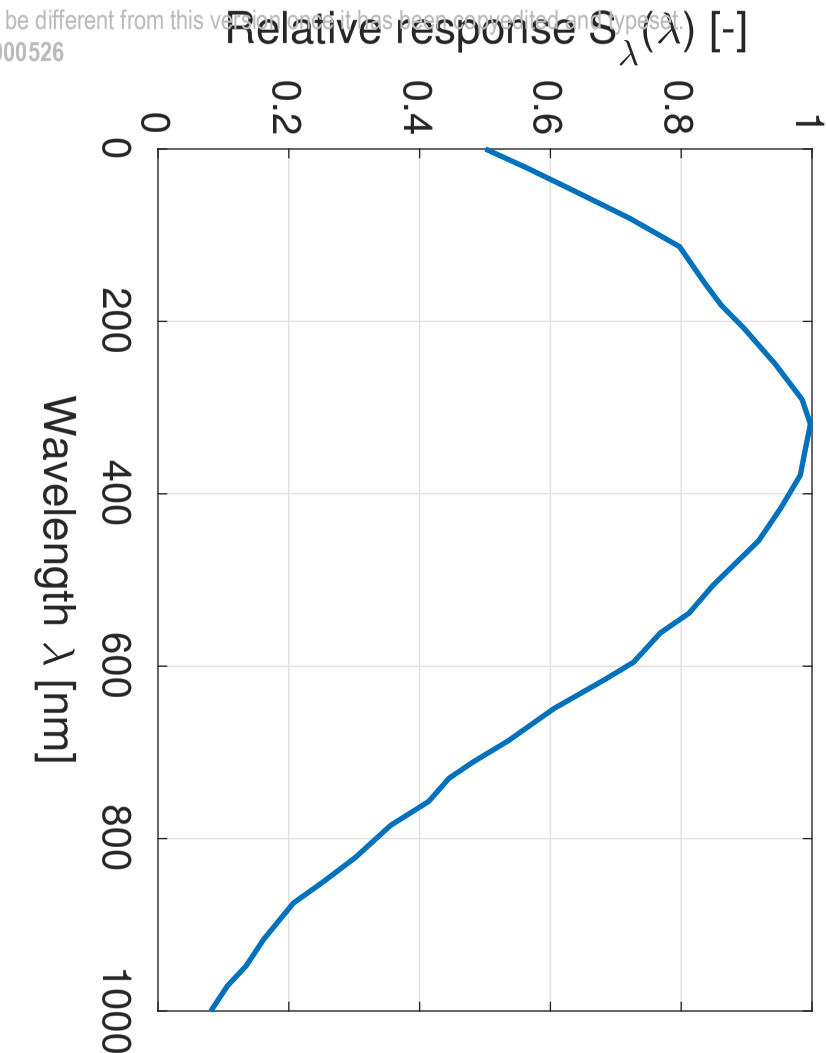

1. FE simulation

2. Artificial image

3. OpenCV post-treatment

AIP Publishing
ALIA THE LASER INSTITUTE
Journal of Laser Applications
ACCEPTED MANUSCRIPT

PLEASE CITE THIS ARTICLE AS DOI: 10.2351/7.0000526